

Article

Detection and 3D Visualization of Deformations for High-Rise Buildings in Shenzhen, China from High-Resolution TerraSAR-X Datasets

Wenqing Wu ¹, Haotian Cui ¹, Jun Hu ^{1,2,*}  and Lina Yao ³

¹ School of Geosciences and Info-physics, Central South University, Changsha 410083, China

² Key Laboratory of Metallogenic Prediction of Nonferrous Metals and Geological Environment Monitoring, Central South University, Ministry of Education, Changsha 410083, China

³ HuaZheng Geospace Information Technology Co., Ltd., Wuhan 430000, China

* Correspondence: csuhujun@csu.edu.cn; Tel.: +86-137-8705-0426

Received: 27 August 2019; Accepted: 9 September 2019; Published: 11 September 2019



Abstract: Shenzhen, a coastal city, has changed from a small village to a supercity since the late 1980s. With the rapid development of its population and economy, ground disasters also occur frequently. These disasters bring great harm to human life and surface architecture. However, there is a lack of regular ground measurement data in this area. Permanent scatterer interferometry (PSI) technology can detect millimeter deformation of urban surface. In this paper, the building height and deformation from 2008 to 2010 in the Futian District of Shenzhen are obtained by using this technique alongside high-resolution TerraSAR-X data. For a visual expression of the result, we export the permanent scatterer (PS) points on buildings to Google Earth for 3D visualization after ortho-rectification of the PS height. Based on the Google Earth 3D model, the temporal and spatial characteristics of the building deformation became obvious. The InSAR measurements show that during the study period, the deformation rates of the Futian area are between -10 and 10 mm/year, and deformation is mainly distributed in a few buildings. These unstable activities can be attributed to human activities and the natural climate, which provides a reference for the local government to carry out a survey of surface deformation, as well as the monitoring and management of urban buildings, in the future.

Keywords: PSI; seasonal displacements; 3D model; Shenzhen

1. Introduction

Due to changes in ground water level, soil physical properties, atmospheric temperatures, wind power, light intensity, and the load and structure of the buildings themselves, high-rise buildings often produce different deformations, including vertical settlement, horizontal displacement, inclined deformation, deflections, and cracks. If the deformation is within a certain range, it can be regarded as a normal phenomenon, but if it exceeds the building bearing capacity, it will reduce the life of buildings, and even endanger their safety. Therefore, the stability and reliability of buildings have become the focus of attention [1–5]. Only by observing the deformation of high-rise buildings regularly and studying their deformation laws can we reasonably predict the degree and mode of their future changes. Then, we can take timely preventive and aftercare measures to ensure the safe use of buildings, and protect the safety of human lives and property. Shenzhen, located in the south-central coastal area of Guangdong Province, China, is a bridge between Hong Kong and the mainland of China. Its “National Central cities Index” ranks fourth in China, and it is rated as a first-tier city in the world by Globalization and World Cities (GaWC). The Futian District of Shenzhen is a large central business district led by the new Shenzhen Convention and Exhibition Center, where several high-rise

office buildings are gathered and serve as the main population gathering places. With the rapid growth in population and economy in Shenzhen, extensive human activities have caused an increase of subsidence related hazard [6–10], thereby bringing great harm to surface buildings. Especially, the uneven deformation of high-rise buildings has had a great impact on the safety of buildings.

Synthetic Aperture Radar Interferometric (InSAR) technology has the advantage of wide range observation, high precision measurement (millimeter level), and high resolution. It also has gradually become an effective tool for urban surface subsidence monitoring and geological hazard surveys [11,12]. In particular, the latest high-resolution radar observation satellites (TerraSAR-X, COSMO_SkyMed, ALOS2, etc.) provide unprecedented high spatial resolution and high-quality images [13], giving us the ability to obtain deformation information for a single building, and setting off an upsurge in urban research [14–17]. From the application of InSAR, land subsidence has been observed all over the world, including Beijing [18], Shanghai [19], Bangkok [20], Mexico City [21], Phoenix [22], and Jakarta [23]. The causes of settlement are different, but their effects are mostly the same. Surface deformation easily destroys buildings and production facilities, hinders construction and resource development, and even causes seawater irrigation. Therefore, continuous monitoring of land subsidence, especially in populous areas like Shenzhen, is of great significance.

Several studies have been carried out in Shenzhen. In [24], the authors combined the interferograms of different tracks to estimate the linear rate map and time series in the Pearl River Delta region, which has a higher time resolution than a single track. In order to study the land subsidence related to reclamation, Xu proposed a small baseline subset InSAR method based on a point target (PT). This new method can not only select high density points but also produce reliable InSAR measurements with full spatial resolution [25]. Another study focused on the effects of external digital elevation model (DEM) on the PS-InSAR results in Shenzhen in several different SAR datasets [26]. Recently, some scholars have become interested in the long-term settlement monitoring and interpretation of the deformation signals in Shenzhen. They have used different InSAR methods to invert the ground deformation, analyze the spatial and temporal characteristics of displacement, and explore the role of human activities on surface evolution [27,28].

Taking Shenzhen as an example, this paper introduces how to use high-resolution SAR images to measure the deformation of urban high-rise buildings. Permanent scatterer interferometry (PSI) technology is used to obtain the deformation time series of the target, and the seasonal displacement and its relationship with the climate are analyzed in detail. Combined with a 3D model of the buildings, the temporal and spatial characteristics of building deformation are analyzed, thereby providing a reference for follow-up urban monitoring and management.

2. Study Area and Used Data

The study area is the Futian District, located in the south-central part of Shenzhen City, with a total area of about 80 square kilometers. This district is a main commercial trade area in Shenzhen, with high-rise buildings and many floating populations (Figure 1). With the rapid development of Shenzhen's economy and society in the last 30 years, the pace of urban construction in Shenzhen has accelerated, leading to the deterioration of land subsidence. Shenzhen is a coastal city, featuring organic sand, clay, silt, and gravel in the underground soil. Its soil is also porous and prone to subsidence. At the same time, the overexploitation of groundwater, the soil compaction, the construction of subway tunnels, and the excavation of large foundation pits of high-rise buildings can disturb the soil. Human activities and natural forces may also cause disaster hazards in this area, so it is necessary to monitor such hazards [24].

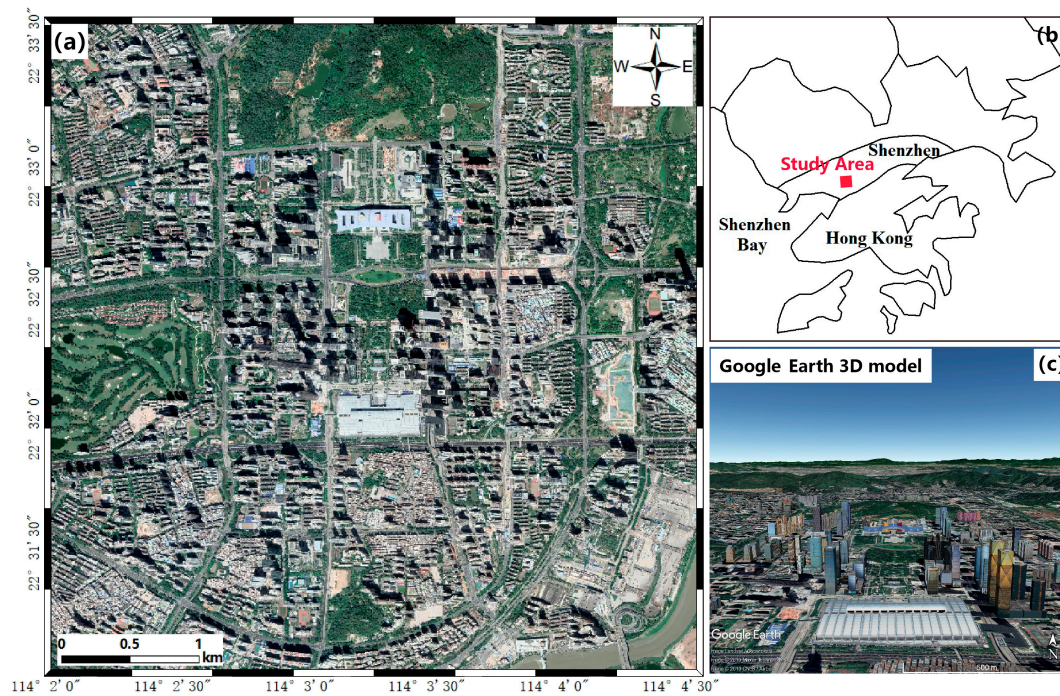


Figure 1. (a) Optical image of the Futian District in Shenzhen, (b) geographic location of study area, and (c) Google Earth 3D model of the Futian District in Shenzhen.

A dataset of the TerraSAR-X images acquired between 2008 and 2010, along the ascending orbit (39 scenes, see Table 1 for detail), were employed to analyze the deformation of Futian District. Observation parameters for all the images were as follows: path numbers, 167; incidence angle, 37.3°; range pixel spacing, 0.9 m; azimuth pixel spacing, 2.0 m; polarization mode, VV. After setting the baseline and coregistration, we obtained 38 image pairs. The maximum spatial baseline is 228 m and the minimum is only 1 m; the time interval of interference pair was set to 11–440 days. Meanwhile, the 30 m resolution SRTM (NASA’s Shuttle Radar Topography Mission) DEM data were used to remove the topographic phases [29].

Table 1. Parameters of the formed image pairs. B and T represent the spatial baseline and time interval between the two acquisitions, respectively.

No.	Master	Slave	B (m)	T (day)	No.	Master	Slave	B (m)	T (day)
1	27 Jul 2009	25 Oct 2008	−155.116	−275	20	27 Jul 2009	01 Oct 2009	114.078	66
2	27 Jul 2009	05 Nov 2008	147.534	−264	21	27 Jul 2009	12 Oct 2009	−139.018	77
3	27 Jul 2009	16 Nov 2008	19.082	−253	22	27 Jul 2009	23 Oct 2009	1.563	88
4	27 Jul 2009	27 Nov 2008	−94.067	−242	23	27 Jul 2009	03 Nov 2009	−103.671	99
5	27 Jul 2009	08 Dec 2008	−96.334	−231	24	27 Jul 2009	14 Nov 2009	46.495	110
6	27 Jul 2009	10 Jan 2009	65.431	−198	25	27 Jul 2009	25 Nov 2009	−78.580	121
7	27 Jul 2009	21 Jan 2009	0.007	−187	26	27 Jul 2009	06 Dec 2009	−92.024	132
8	27 Jul 2009	01 Feb 2009	−77.118	−176	27	27 Jul 2009	17 Dec 2009	9.598	143
9	27 Jul 2009	12 Feb 2009	152.038	−165	28	27 Jul 2009	06 Apr 2010	16.349	253
10	27 Jul 2009	23 Feb 2009	−132.662	−154	29	27 Jul 2009	11 Jun 2010	15.189	319
11	27 Jul 2009	06 Mar 2009	−50.314	−143	30	27 Jul 2009	22 Jun 2010	78.681	330
12	27 Jul 2009	17 Mar 2009	51.370	−132	31	27 Jul 2009	03 Jul 2010	138.544	341
13	27 Jul 2009	30 Apr 2009	51.719	−88	32	27 Jul 2009	14 Jul 2010	78.968	352
14	27 Jul 2009	11 May 2009	31.028	−77	33	27 Jul 2009	25 Jul 2010	228.633	363
15	27 Jul 2009	22 May 2009	26.786	−66	34	27 Jul 2009	16 Aug 2010	−58.890	385
16	27 Jul 2009	02 Jun 2009	−8.321	−55	35	27 Jul 2009	07 Sep 2010	−23.908	407
17	27 Jul 2009	24 Jun 2009	226.309	−33	36	27 Jul 2009	18 Sep 2010	−192.315	418
18	27 Jul 2009	05 Jul 2009	106.160	−22	37	27 Jul 2009	29 Sep 2010	139.579	429
19	27 Jul 2009	16 Jul 2009	−41.524	−11	38	27 Jul 2009	10 Oct 2010	50.539	440

3. Methodology

3.1. Permanent Scatterer Interferometry (PSI) Data Processing

Since the D-InSAR technology is susceptible to atmospheric phase delays and incoherence [30,31], Ferretti presented a time-series InSAR technique based on permanent scatterer interferometry (PSI) and extended it to a nonlinear deformation mode [32,33]. PSI is a technique for obtaining surface deformation information through long-time stable reflection points (i.e., PS points, such as artificial buildings, exposed rock, and sand) [34–36]. By unwrapping the PS network, the interference of the atmosphere on the deformation phase can be greatly reduced, and the residual atmosphere and noise phases can also be removed or weakened by space-time filtering, so we can retrieve high precision surface deformation.

For the phase value of any pixel (x, y) in a differential interferogram (T_i) , we assume that the deformation is made up of linear and nonlinear parts that are consistent in urban environments [37,38]:

$$\Phi_i(x, y, T_i) = -\frac{4\pi}{\lambda \cdot R \cdot \sin \theta} \cdot B_i^\perp \cdot \varepsilon(x, y) - \frac{4\pi}{\lambda} \cdot T_i \cdot v(x, y) - a \cdot \frac{4\pi}{\lambda} \cdot \sin(2\pi \cdot T_i) + \varphi_i^{\text{res}}(x, y, T_i) \tag{1}$$

where

$$\varphi_i^{\text{res}}(x, y, T_i) = \varphi_i^{\text{nl}}(x, y, T_i) + \varphi_i^{\text{a}}(x, y, T_i) + \varphi_i^{\text{n}}(x, y, T_i) \tag{2}$$

Here, B_i^\perp , T_i are the spatial perpendicular baseline and time interval of the interference pair, respectively; λ , R , θ represent wavelength, slant distance, and local incident angle of the target point, respectively; $v(x, y)$, $\varepsilon(x, y)$ are the linear deformation rate in line of sight and height error of pixel (x, y) , and a is the amplitude of seasonal deformation; and $\varphi_i^{\text{res}}(x, y, T_i)$ is a complex of the residual deformation phase, the atmospheric delay phase, and the noise phase.

After constructing the network of PSs according to the regulation, the phase increment value between each arc can be obtained by using the difference method, which can be expressed as follows:

$$\begin{aligned} \Delta\Phi_i(x_p, y_p; x_q, y_q, T_i) &= -\frac{4\pi}{\lambda \cdot \overline{R} \cdot \overline{\sin \theta}} \cdot \overline{B_i^\perp} \cdot \Delta\varepsilon(x_p, y_p; x_q, y_q) - \frac{4\pi}{\lambda} \cdot T_i \cdot \Delta v(x_p, y_p; x_q, y_q) \\ &\quad - \Delta a(x_p, y_p; x_q, y_q) \cdot \frac{4\pi}{\lambda} \cdot \sin(2\pi \cdot T_i) \\ &\quad + \Delta\varphi_i^{\text{res}}(x_p, y_p; x_q, y_q, T_i) \end{aligned} \tag{3}$$

where $\overline{B_i^\perp}$, \overline{R} , $\overline{\theta}$ are the average values of the corresponding parameters of the adjacent PS points p and q , $\Delta\varepsilon$, Δv , Δa are the height error increment, the linear deformation rate increment, and the seasonal deformation amplitude increment, respectively; $\Delta\varphi_i^{\text{res}}$ shows the increment of the corresponding residual phase.

Under the condition of $\Delta\varphi_i^{\text{res}} < \pi$, the parameters $(\Delta\varepsilon, \Delta v, \Delta a)$ can be estimated from M wrapped differential interferograms. At this time, the maximum optimization value of the following functions can be used to obtain the above unknowns:

$$\gamma = \left| \frac{1}{M} \sum_{i=1}^M (\cos \Delta\omega_i + j \cdot \sin \Delta\omega_i) \right| = \max \tag{4}$$

where

$$\Delta\omega_i = \Delta\Phi_i - \frac{4\pi}{\lambda \cdot \overline{R} \cdot \overline{\sin \theta}} \cdot \overline{B_i^\perp} \cdot \Delta\varepsilon - \frac{4\pi}{\lambda} \cdot T_i \cdot \Delta v - \Delta a \cdot \frac{4\pi}{\lambda} \cdot \sin(2\pi \cdot T_i) \tag{5}$$

Here, γ is the ensemble temporal coherence and $\Delta\omega_i$ indicates the difference between the observation and the fitted value. By searching in a three-dimensional space, each arc is estimated by using the maximum ensemble coherence (solution space search method), and the height error and deformation rate of the corresponding arc segment can be obtained. Then, the global integration of

difference increment value is carried out, so the height error and deformation rate can be determined at each node of the network.

3.2. Ortho-Rectification and 3D Visualization

Compared with D-InSAR, another advantage of PS-InSAR technology is that it cannot only estimate the deformation rate but can also obtain the height error of each PS. Combined with the external DEM, the SAR image pixel can be accurately located in a three-dimensional space. Medium-resolution images are limited by resolution. They can acquire little semantic information on the ground, making it difficult to display a single building. However, under a high resolution, there will be multiple PS points on a single building, which makes it possible to measure the deformation of a single building. In this case, the traditional two-dimensional InSAR can no longer meet the application needs of urban three-dimensional information display, and a 3D visualization of building deformation emerges, as required.

After geocoding, determining how to “stand” PSs in a three-dimensional space (despite the side-looking imaging features of the SAR satellite) is a problem that must be considered in high-resolution PS-InSAR. In the geometry of SAR imaging, the height of a building is the main reason for side-looking projection. By correcting the coordinates of PSs projected to the ground in a three-dimensional space, the real spatial position can be restored. Supposing a spatial coordinate system $O - XYZ$, h is the building height, with a PS point at the top of the building (Figure 2). The local incident angle of the radar wave is θ , which produces a projection along the ground range direction, and α is the angle between the projection of the building and the X axis, which we also call the azimuth. The real spatial coordinates of the PS point are (x, y, h) , and the projected ground coordinates are $(x_1, y_1, 0)$. According to the relationship expressed in Figure 2, the following formula can be established:

$$\begin{cases} x = x_1 + h \cdot \cos \alpha / \tan \theta \\ y = y_1 + h \cdot \sin \alpha / \tan \theta \end{cases} \quad (6)$$

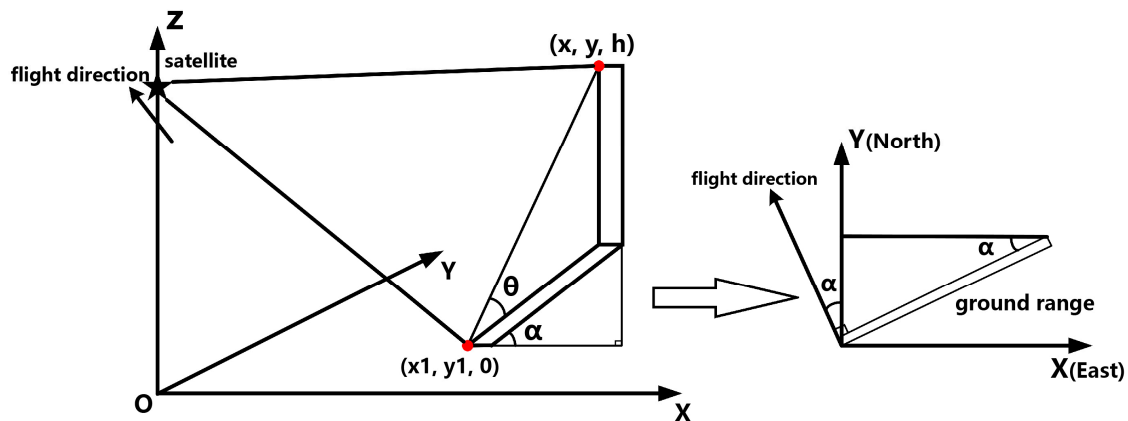


Figure 2. Schematic diagram of ortho-rectification.

Finishing the above operation, the height of the PS points on the building can be restored. This is also called ortho-rectification of the PS points.

Three-dimensional visualization is a tool for describing and understanding the characteristics of many geological phenomena on the ground and underground and is widely used in all fields of geology and geophysics. InSAR 3D visualization is conducive to accurately and rapidly describing various complex ground deformation phenomena. Most of the previous PSI monitoring results are displayed in a two-dimensional plane, which is inconsistent with the characteristics of urban three-dimensional buildings, so it is difficult to correctly explain the causes of deformation. In high-resolution images,

PS points can be densely distributed in various parts of the building (excluding the shadow surface), making PS points convenient to analyze the stress and strain status of buildings. After ortho-rectification, accurate longitude, latitude, and height coordinates for the PS points can be obtained, and we can use these coordinates on the building. Combined with an actual 3D building model, the temporal and spatial characteristics of the building deformation can be analyzed. The main flow is as shown in Figure 3. In addition to conventional PSI operations, we have also added ortho-rectification and 3D visualization, which are unique to high-resolution SAR data processing.

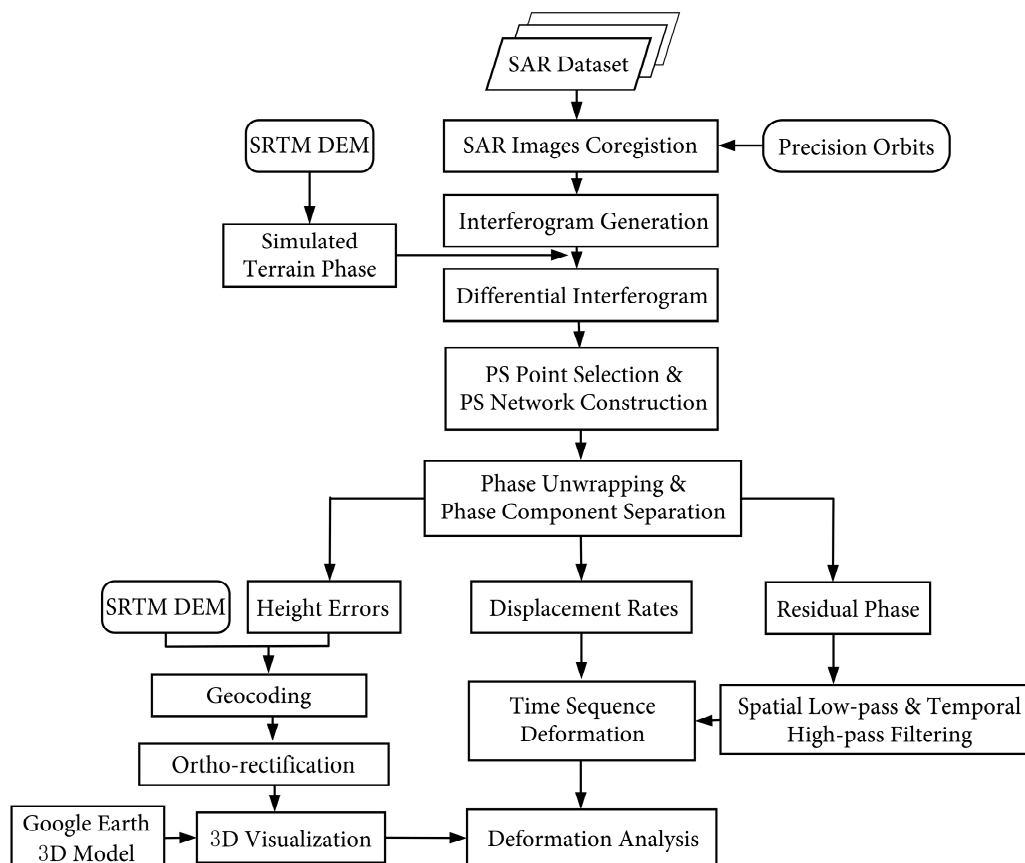


Figure 3. Flowchart of high-resolution permanent scatterer interferometry (PSI) deformation monitoring.

4. Experiments and Results

4.1. Results of the PSI

The data processing begins with a stack of single-look complex images (SLC). Based on the single reference image mode, the image acquired on 27 July 2009 is selected as a reference image, and the others are registered with it to form interferograms. The terrain phase is simulated by a 30 m resolution SRTM DEM, and 38 single-look differential interferograms are finally obtained.

The purpose of this experiment is to monitor the deformation of the building, so it is necessary to accurately determine the permanent scatterers on typical buildings in the study area and ensure a certain density to establish a three-dimensional model. In this experiment, the coherent coefficient and amplitude deviation indexes are used to detect PSs. A small threshold is used first to extract the PS candidate points, which can filter out certain regions, such as watery areas, vegetation, and other areas with low-coherence, and improve the accuracy of the second selection. See Figure 4, where the green points are detected PSs, which are placed on an intensity image. The number of PS points finally extracted is 108,139, the point density is about 18,023 PS/km², and the main region is well covered. The red dot on the road is the reference point for unwrapping, with little effects on the PSI results.

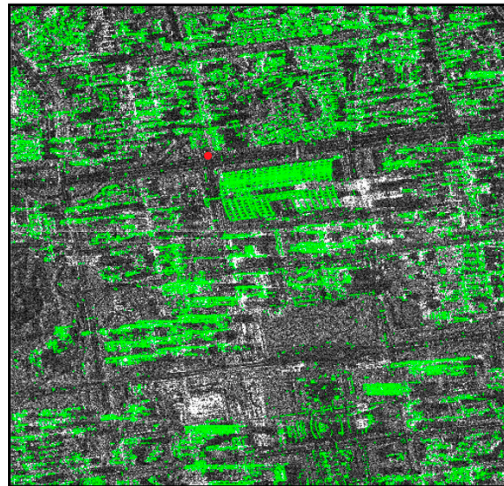


Figure 4. Permanent scatterer (PS) points distribution map. Red dot is the reference point for the unwrapping.

The final PSI results are shown in Figure 5, where Figure 5a is the absolute elevation of the building, ranging from 0 m to 250 m. The height estimated by the PSI is consistent with the height of the actual building model. In the deformation rate map (Figure 5b), the deformation rates, fitted by linear and nonlinear deformation, are mainly between -10 mm/year and 10 mm/year. Most of the buildings tend to be stable, but we also observed some signs of deformation. The most obvious deformation occurred in the Shenzhen International Convention and Exhibition Center, the top of which has a large area uplift trend. We suspect that this trend is related to thermal expansion, and we will analyze it later.

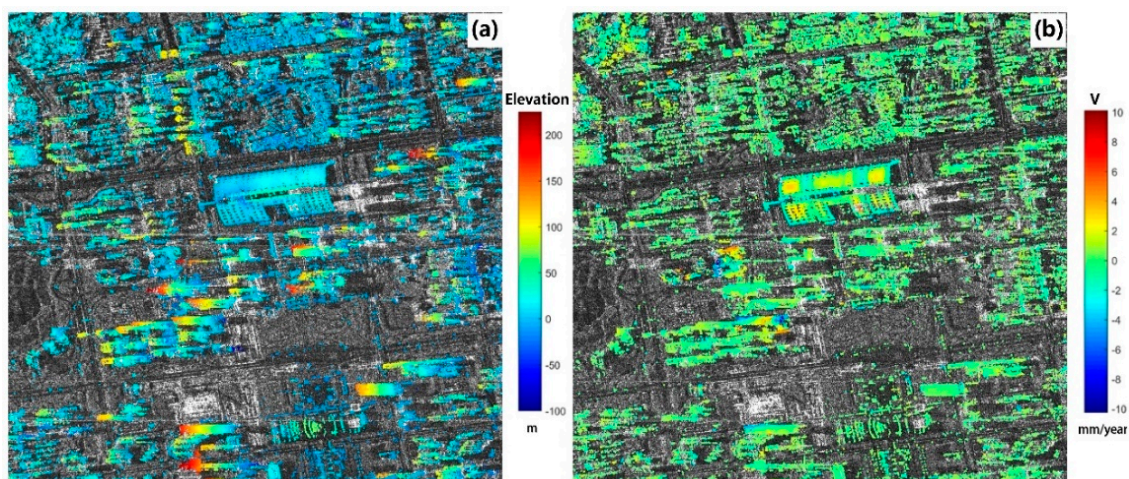


Figure 5. The absolute elevation map (a) and deformation rate map (b) of the study area; the elevation is calculated by combining the SRTM (NASA's Shuttle Radar Topography Mission) DEM and the height error.

4.2. Results of 3D Visualization

High resolution data have a stronger ability to display detail, and PS points can be accurately positioned on the building after ortho-rectification [39,40]. Therefore, taking the buildings in the Futian District of Shenzhen as the research goal, the elevation information of the PS points is imported into Google Earth for 3D visualization using the keyhole markup language (KML). Three-dimensional visualization can significantly improve the presentation ability of the results and can also verify the

accuracy of the deformation by measuring the results from the side. See Figure 6, where the picture above shows all the “standing” PS points in the study area, and the following highlight the three landmarks: Figure 6b–d. The color represents their height values, and all of them are placed on the 3D building model from Google Earth. The PS height estimated by PSI has a high similarity with the 3D model, which can help facilitate the 3D reconstruction of urban buildings [41,42].

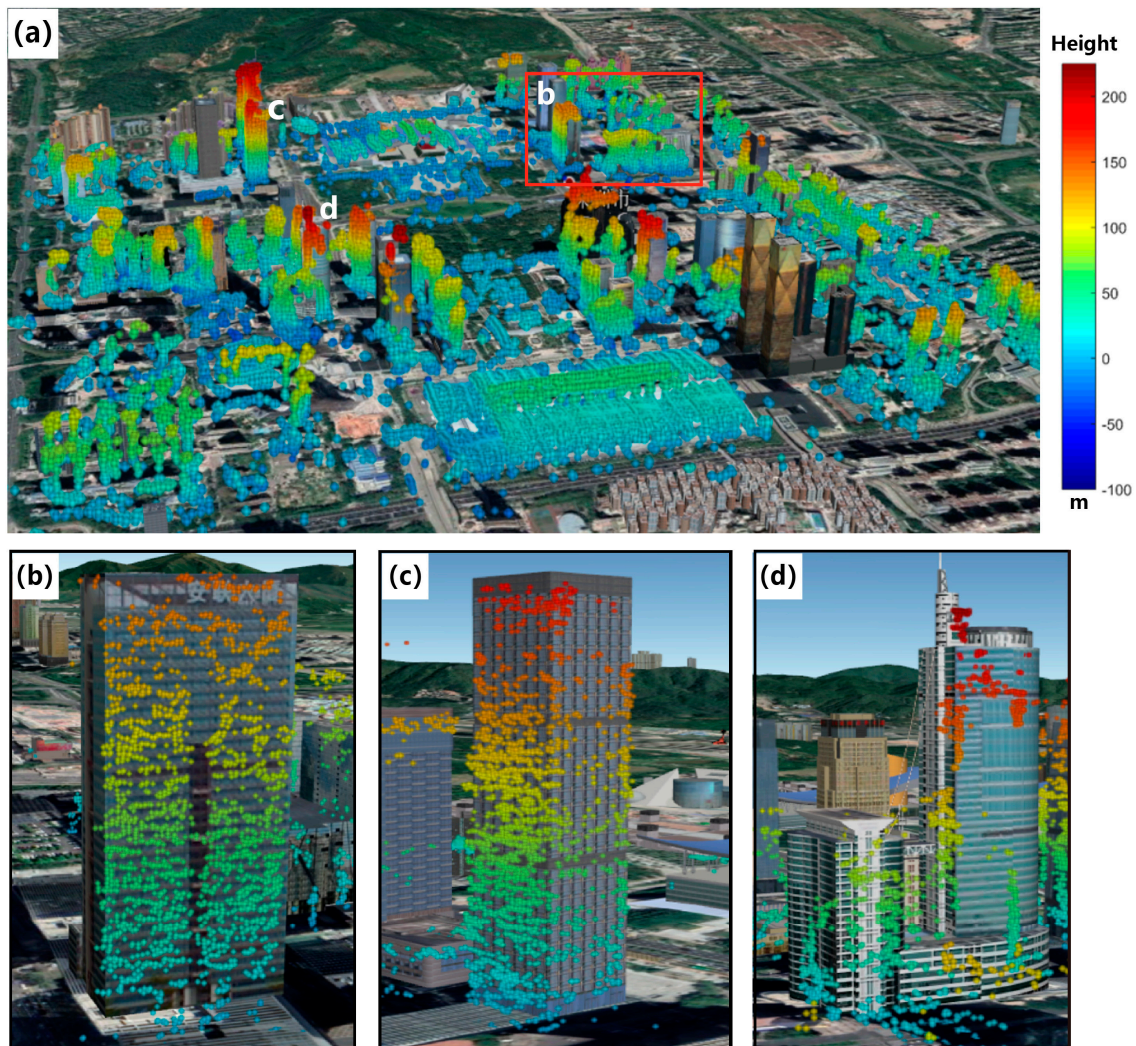


Figure 6. Three-dimensional visualization results of the PS height. (a) The panoramic view of PS height in the study area and (b–d) the local magnification of buildings (b), (c), and (d), respectively. The red rectangle represents the FengHuang building.

However, an interesting phenomenon was found. Figure 7 shows three-dimensional pictures of the FengHuang building. We found that the model built in Google Earth does not match the real scene map, and the PS point height we extracted is closer to that of the actual building. Therefore, the accuracy of the Google Earth 3D model can be verified by the 3D visualization of the PS height, which has not been mentioned in previous experiments.

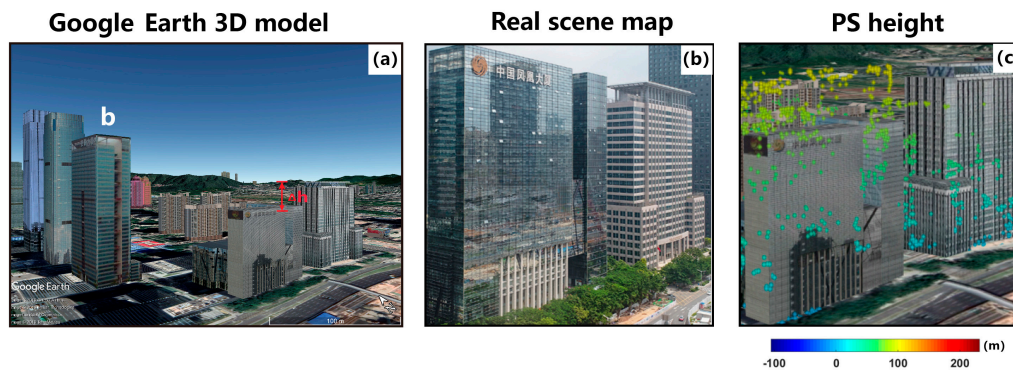


Figure 7. (a) The Google Earth 3D model of the FengHuang building in Figure 6 and (b) its real scene map; (c) the three-dimensional representations of the extracted PS point heights geocoded in the Google Earth 3D model.

By using PSI technology and a 3D visualization platform, an accurate deformation monitoring system can be established for high-rise buildings in urban areas. Figure 8 is a three-dimensional view of the PS point deformation rates, which can intuitively and completely read the deformation results of the high-rise buildings from top to bottom. On the three-dimensional map, the deformation of key parts of the high-rise building can be analyzed carefully, and we will get a comprehensive understanding of the health status of urban buildings. From the LOS deformation rate map, the overall performance is good. Except for the obvious adverse reactions of the four buildings, most of the buildings are stable. Next, we will analyze and discuss buildings with obvious deformation.

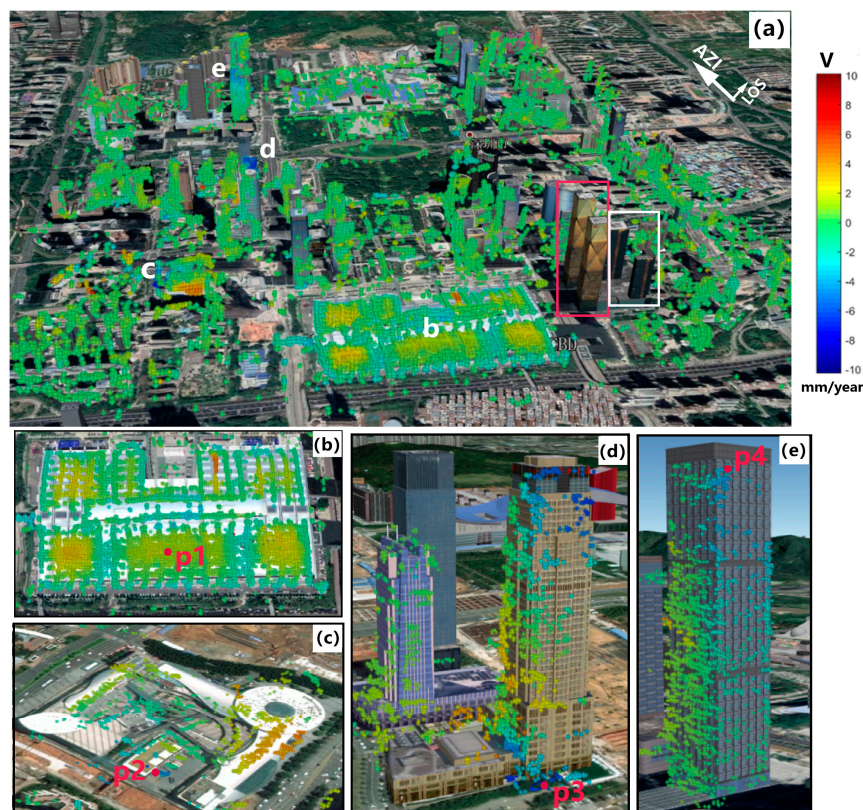


Figure 8. Three-dimensional visualization results of the PS deformation rates. (a) The panoramic view of PS deformation rates in study area; (b–e) the local magnification of buildings b, c, d, e; the red points p1, p2, p3, and p4 are four deformation feature points on the buildings, and the boxes contain some buildings without PS points.

5. Discussion

Shenzhen is in the south-central coastal area of Guangdong Province. With low latitudes, its climate is a subtropical marine climate characterized by hot and rainy summers and mild and dry winters. Its annual average temperature is 22.4 °C, its maximum temperature is 38.7 °C (10 July 1980), and its minimum temperature is 0.2 °C (11 February 1957). There is a long period of sunshine, with average annual sunshine of 2120.5 h and annual solar radiation of 5225 megajoules per square meter. Long-term solar radiation and high temperatures can easily lead to an increase in object volume and thermal expansion effect. Of course, this situation is not sustained, seasonal changes will make thermal expansion a cyclical behavior.

Figure 8b features the Shenzhen Convention and Exhibition Center, the largest single building in Shenzhen, whose top is a combination of a steel structure and glass. The glass has a certain thermal expansion coefficient and is susceptible to changes in temperature. We obtained the time sequence deformation of point p1 in the Convention and Exhibition Center and compared it with the monthly average temperature change in this area (Figure 9a). The seasonal trend of the exhibition center is obvious and is consistent with the temperature changes. In summer, the expansion of the convention center goes up to 15 mm and is affected by high temperatures. In the long term, there may also be a linear lift trend of about 2 mm/year. Figure 8c,d is a shopping center and a commercial building. From the time sequence deformation results of points p2 and p3 in Figure 9b,c, the settlement of those two parts is obvious during the study period. Overextraction of groundwater, soil compaction, great pressure of high-rise buildings, continuous action of ground load, and underground construction may lead to such deformation. In order to understand the causes of settlement of these two buildings, drilling data and geological maps are also needed.

Figure 8e is an office building in the Futian District. According to the deformation time series of p4 (Figure 9d), the cause of deformation is more likely to be affected by wind force. In Shenzhen, due to the influence of monsoons, the southeast wind prevails during the summer. As a coast city, Shenzhen is affected by tropical cyclones (typhoons) 4–5 times a year, and strong winds with wind speeds greater than 17 m/s (grade 8) occur about 4 days a year, mainly during summer and autumn. Of these winds, 39% occur in July and August, and only 7% occur in winter and spring. When a strong wind strikes, high-rise buildings wobble with an amplitude of 1–2 cm; it is normal to feel a slight sloshing in those buildings.

We also found that there are no PS points on some buildings in Figure 8. Based on the geometry of the image, electromagnetic waves can propagate directly and radiate to the buildings in the red box, so the absence of PS points may be related to their materials. The buildings in the white box may be affected by shadows [43–45]. Radar detection in urban areas is relatively complex because of the prevalence of layover and shadows. A small incident angle produces a poor range resolution, while a large incident angle increases the range of the radar shadow, which can cover up an urban building. Therefore, when monitoring urban deformation, it is necessary to select an appropriate radar incident angle according to our research target.

In general, the deformation of the Futian District is within an allowable range, except for a few buildings. Of course, this is only an early result. In order to keep up with the pace of development in Shenzhen, new data must be used.

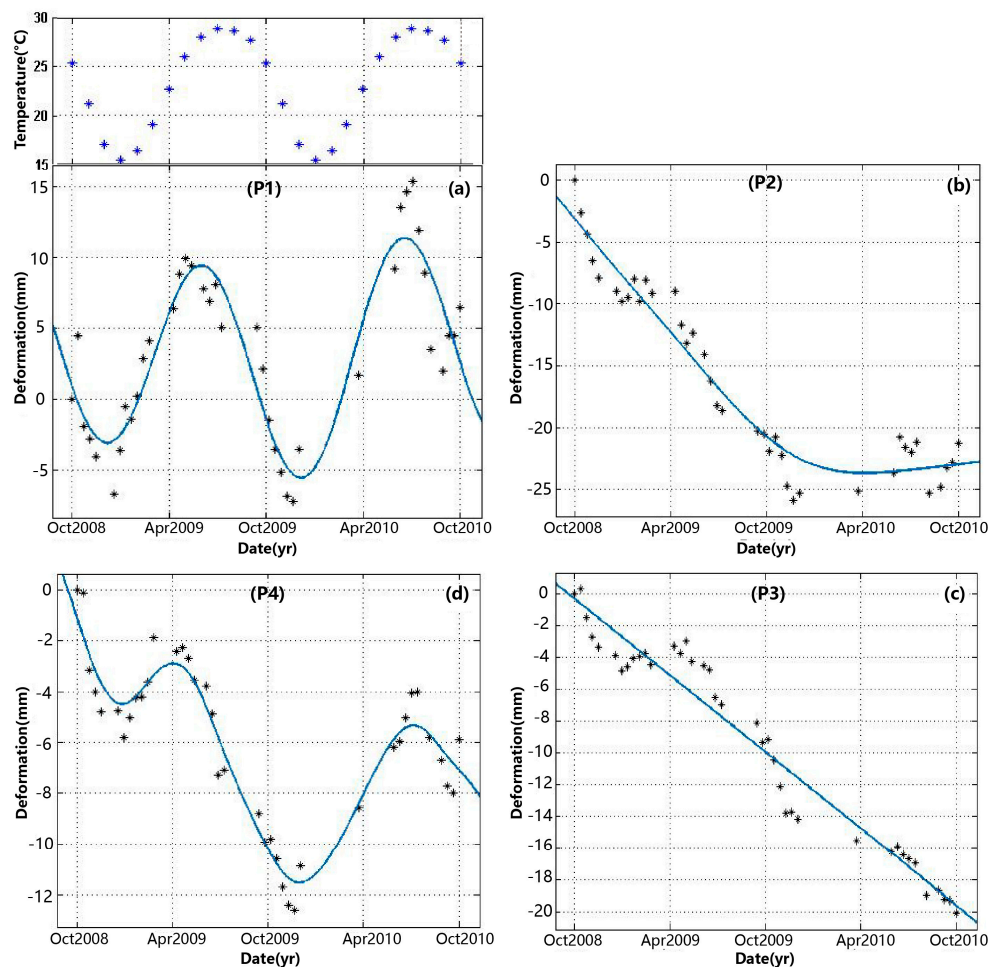


Figure 9. Deformation time series of four feature points in Figure 8. (a–d) The deformation time series of p1, p2, p3, and p4, respectively.

6. Conclusions

In this paper, the deformation of the Futian District of Shenzhen City from 2008 to 2010 was obtained by the high-resolution TerraSAR-X data and PSI techniques. For a visual expression of the results, we exported the PS points of the buildings to Google Earth for 3D visualization after ortho-rectification of the PS height. Based on the Google Earth 3D model, the temporal and spatial characteristics of the building deformation became obvious. The deformation analysis results showed that during the study period, the deformation rates of the Futian area were between -10 and 10 mm/year. Most of the regions were stable, and the deformation was mainly distributed in a few buildings. We found that the Shenzhen International Convention and Exhibition Center showed seasonal deformation, which was related to changes in local temperature. A rise in the temperature results in an expansion of the building, while a decrease in temperature compresses it. In addition, high-rise buildings are vulnerable to strong winds, which are regular and acceptable because winds are considered at the beginning of construction. There were also some discordant phenomena. For example, two buildings displayed obvious settlement. Since only the TerraSAR-X data can be acquired for the study area, the definition of driving mechanism of buildings' deformation is not within the scope of this study. Deformation causation investigation can be conducted in the future when the additional data is available.

Since only the ascending data were available, this experiment did not involve the other side of buildings, and some buildings were missed due to their materials and shadows. Furthermore, widespread layover and shadow in urban areas can easily lead to the lack of building shape, and we'll

get nothing from the missing part of the buildings. Therefore, fusing multi-source data to obtain comprehensive building deformation information will be the next stage in our work.

Author Contributions: W.W. and J.H. conceived and designed the experiments; W.W. and H.C. performed the experiments; J.H. and L.Y. analyzed the results. W.W. wrote the paper. All authors reviewed and approved the manuscript.

Funding: This research received no external funding.

Acknowledgments: We appreciate Infoterra GmbH and USGS for providing TerraSAR-X SAR images and SRTM DEM. This work was supported by the National Key Basic Research and Development Program of China (No. 2018YFC1505101), the National Natural Science Foundation of China (Nos. 41674010, 41774023), the Science and Technology Project of Hunan Province (Nos. 2018JJ3347, 2017RS3001), and the Project of Education Department of Hunan Province (No. 16K053).

Conflicts of Interest: The authors declare no conflict of interest.

References

1. Wang, D.; Lu, X.Z.; Zhang, Z.J.; Pan, Q.L.; Wang, S.L.; Wang, B.F.; Liu, G.Y.; Zhang, F.L.; Yan, X.P.; Ou, H.P. *JGJ8–2007, Code for Deformation Measurement of Building and Structure*; China Architecture and Building Press: Beijing, China, 2007; pp. 32–40.
2. Bru, G.; Herrera, G.; Tomás, R.; Duro, J.; Dela, V.R.; Mulas, J. Control of deformation of buildings affected by subsidence using persistent scatterer interferometry. *Struct. Infrastruct. Eng.* **2010**, *9*, 188–200. [[CrossRef](#)]
3. Frattini, P.; Crosta, G.B.; Allievi, J. Damage to buildings in large slope rock instabilities monitored with the PSInSAR™ technique. *Remote Sens.* **2013**, *5*, 4753–4773. [[CrossRef](#)]
4. Ciampalini, A.; Bardi, F.; Bianchini, S.; Frodella, W.; del Ventisette, C.; Moretti, S.; Casagli, N. Analysis of building deformation in landslide area using multisensor PSInSAR™ technique. *Int. J. Appl. Earth Obs. Geoinform.* **2014**, *33*, 166–180. [[CrossRef](#)] [[PubMed](#)]
5. Yang, K.; Yan, L.; Huang, G.; Chen, C.; Wu, Z. Monitoring Building Deformation with InSAR: Experiments and Validation. *Sensors* **2016**, *16*, 12. [[CrossRef](#)] [[PubMed](#)]
6. Lai, L.W.; Lu, W.W.; Lorne, F.T. A catallactic framework of government land reclamation: The case of Hong Kong and Shenzhen. *Habitat Int.* **2014**, *44*, 62–71. [[CrossRef](#)]
7. China Daily. Shenzhen Eyes Land Reclamation to Curb Rising Housing Price. 2016. Available online: http://www.chinadaily.com.cn/china/2016-03/04/content_23738729.htm (accessed on 25 September 2017).
8. South China Morning Post. Reclamation Threatens Last of Shenzhen's Coastline. 2010. Available online: <http://www.scmp.com/article/719552/reclamation-threatens-last-shenzhens-coastline> (accessed on 25 September 2017).
9. IFENG. Subsidence of Buildings in Land Reclamation Area of Shenzhen, with Cracks Found on Pavements. 2010. Available online: <http://finance.ifeng.com/city/sz/20100402/2003288.shtml> (accessed on 25 September 2017).
10. IFENG. Subsidence Due to Metro Construction in Shenzhen, with Cracks Opening up over Buildings. 2010. Available online: http://news.ifeng.com/mainland/detail_2010_05/21/1539325_0.shtml (accessed on 25 September 2017).
11. Du, Y.N.; Feng, G.C.; Peng, X.; Li, Z.W. Subsidence Evolution of the Leizhou Peninsula, China, Based on InSAR Observation from 1992 to 2010. *Appl. Sci.* **2017**, *7*, 466. [[CrossRef](#)]
12. Zhang, L.; Sun, Q.; Hu, J. Potential of TCPInSAR in Monitoring Linear Infrastructure with a Small Dataset of SAR Images: Application of the Donghai Bridge, China. *Appl. Sci.* **2018**, *8*, 425. [[CrossRef](#)]
13. Jo, M.J.; Jung, H.S.; Won, J.S. Measurement of precise three-dimensional volcanic deformations via TerraSAR-X synthetic aperture radar interferometry. *Remote Sens. Environ.* **2017**, *192*, 228–237. [[CrossRef](#)]
14. Adam, N.; Zhu, X.; Bamler, R. Coherent stacking with TerraSAR-X imagery in urban areas. In Proceedings of the 2009 Joint Urban Remote Sensing Event, Shanghai, China, 20–22 May 2009; pp. 1–6.
15. Bianchini, S.; Pratesi, F.; Nolesini, T.; Casagli, N. Building deformation assessment by means of persistent scatterer interferometry analysis on a landslide-affected area: The Volterra (Italy) case study. *Remote Sens.* **2015**, *7*, 4678–4701. [[CrossRef](#)]
16. Gernhardt, S.; Adam, N.; Eineder, M.; Bamler, R. Potential of very high-resolution SAR for persistent scatterer interferometry in urban areas. *Ann. GIS* **2010**, *16*, 103–111. [[CrossRef](#)]

17. Gernhardt, S.; Bamler, R. Deformation monitoring of single buildings using meter-resolution SAR data in PSI. *ISPRS J. Photogramm. Remote Sens.* **2012**, *73*, 68–79. [[CrossRef](#)]
18. Hu, B.; Wang, H.S.; Sun, Y.L.; Hou, J.G.; Liang, J. Long-Term Land Subsidence Monitoring of Beijing (China) Using the Small Baseline Subset (SBAS) Technique. *Remote Sens.* **2014**, *6*, 3648–3661. [[CrossRef](#)]
19. Pepe, A.; Bonano, M.; Zhao, Q.; Yang, T.; Wang, H. The Use of C-/X-Band Time-Gapped SAR Data and Geotechnical Models for the Study of Shanghai's Ocean-Reclaimed Lands through the SBAS-DInSAR Technique. *Remote Sens.* **2016**, *8*, 911. [[CrossRef](#)]
20. Aobpaet, A.; Cuenca, M.C.; Hooper, A.; Trisirisatayawong, I. InSAR time-series analysis of land subsidence in Bangkok, Thailand. *Int. J. Remote Sens.* **2013**, *34*, 2969–2982. [[CrossRef](#)]
21. Castellazzi, P.; Martel, R.; Rivera, A.; Huang, J.; Pavlic, G.; Calderhead, A.I.; Chaussard, E.; Garfias, J.; Salas, J. Groundwater depletion in Central Mexico: Use of GRACE and InSAR to support water resources management. *Water Resour. Res.* **2016**, *52*, 5985–6003. [[CrossRef](#)]
22. Miller, M.M.; Shirzaei, M. Spatiotemporal characterization of land subsidence and uplift in Phoenix using InSAR time series and wavelet transforms. *J. Geophys. Res. Solid Earth.* **2015**, *120*, 5822–5842. [[CrossRef](#)]
23. Chaussard, E.; Amelung, F.; Abidin, H.; Hong, S.H. Sinking cities in Indonesia: ALOS PALSAR detects rapid subsidence due to groundwater and gas extraction. *Remote Sens. Environ.* **2013**, *128*, 150–161. [[CrossRef](#)]
24. Wang, H.; Wright, T.J.; Yu, Y.; Lin, H.; Jiang, L.; Li, C.; Qiu, G. InSAR reveals coastal subsidence in the Pearl River Delta, China. *Geophys. J. Int.* **2012**, *191*, 1119–1128. [[CrossRef](#)]
25. Xu, B.; Feng, G.; Li, Z.; Wang, Q.; Wang, C.; Xie, R. Coastal Subsidence Monitoring Associated with Land Reclamation Using the Point Target Based SBAS-InSAR Method: A Case Study of Shenzhen, China. *Remote Sens.* **2016**, *8*, 652. [[CrossRef](#)]
26. Du, Y.; Feng, G.; Li, Z.; Peng, X.; Zhu, J.; Ren, Z. Effects of External Digital Elevation Model Inaccuracy on StaMPS-PS Processing: A Case Study in Shenzhen, China. *Remote Sens.* **2017**, *9*, 1115. [[CrossRef](#)]
27. Liu, P.; Chen, X.; Li, Z.; Zhang, Z.; Xu, J.; Feng, W.; Wang, C.; Hu, Z.; Tu, W.; Li, H. Resolving surface displacements in Shenzhen of China from time series InSAR. *Remote Sens.* **2018**, *10*, 1162. [[CrossRef](#)]
28. Hu, B.; Chen, J.; Zhang, X. Monitoring the Land Subsidence Area in a Coastal Urban Area with InSAR and GNSS. *Sensors* **2019**, *19*, 3181. [[CrossRef](#)] [[PubMed](#)]
29. Farr, T.G.; Kobrick, M. Shuttle radar topography mission produces a wealth of data. *Eos Trans.* **2000**, *81*, 583–585. [[CrossRef](#)]
30. Hu, J.; Li, Z.W.; Ding, X.L.; Zhu, J.J.; Zhang, L.; Sun, Q. Resolving three-dimensional surface displacements from InSAR measurements: A review. *Earth Sci. Rev.* **2014**, *133*, 1–17. [[CrossRef](#)]
31. Jung, H.S.; Lu, Z.; Won, J.S.; Poland, M.P.; Miklius, A. Mapping three-dimensional surface deformation by combining multiple-aperture interferometry and conventional interferometry: Application to the June 2007 eruption of Kilauea volcano, Hawaii. *IEEE Geosci. Remote Sens. Lett.* **2011**, *8*, 34–38. [[CrossRef](#)]
32. Ferretti, A.; Prati, C.; Rocca, F. Permanent Scatterers in SAR interferometry. *IEEE Trans. Geosci. Remote Sens.* **2001**, *39*, 8–20. [[CrossRef](#)]
33. Ferretti, A.; Prati, C.; Rocca, F. Nonlinear subsidence rate estimation using permanent scatterers in differential SAR interferometry. *IEEE Trans. Geosci. Remote Sens.* **2000**, *38*, 2202–2212. [[CrossRef](#)]
34. Hooper, A.; Zebker, H.; Segall, P.; Kampes, B. A new method for measuring deformation on volcanoes and other natural terrains using InSAR persistent scatterers. *Geophys. Res. Lett.* **2004**, *31*, L23611. [[CrossRef](#)]
35. Zhang, L.; Ding, X.L.; Lu, Z. Ground settlement monitoring based on temporarily coherent points between two SAR acquisitions. *ISPRS J. Photogramm. Remote Sens.* **2011**, *66*, 146–152. [[CrossRef](#)]
36. Zhang, L.; Lu, Z.; Ding, X.L.; Jung, H.S.; Feng, G.C.; Lee, C.W. Mapping ground surface deformation using temporarily coherent point SAR interferometry: Application to Los Angeles Basin. *Remote Sens. Environ.* **2012**, *117*, 429–439. [[CrossRef](#)]
37. Zhu, X.X. Very High-Resolution Tomographic SAR Inversion for Urban Infrastructure Monitoring—A Sparse and Nonlinear Tour. Ph.D. Thesis, Technische Universität München, München, Germany, 2011.
38. Montazeri, S. The Fusion of SAR Tomography and Stereo-SAR for 3D Absolute Scatterer Positioning. Master's Thesis, Delft University of Technology, Delft, The Netherlands, 2014.
39. Balss, U.; Cong, X.Y.; Brcic, R.; Rexer, M.; Minet, C.; Breit, H.; Eineder, M.; Fritz, T. High precision measurement on the absolute localization accuracy of TerraSAR-X. In Proceedings of the 2012 IEEE International Geoscience and Remote Sensing Symposium (IGARSS), Munich, Germany, 22–27 July 2012; pp. 1625–1628.

40. Montazeri, S.; Gisinger, C.; Eineder, M.; Zhu, X.X. Automatic Detection and Positioning of Ground Control Points Using TerraSAR-X Multiaspect Acquisitions. *IEEE Trans. Geosci. Remote Sens.* **2018**, *56*, 2613–2632. [[CrossRef](#)]
41. Duque, S.; Breit, H.; Balss, U.; Parizzi, A. Absolute Height Estimation Using a Single TerraSAR-X Staring Spotlight Acquisition. *IEEE Geosci. Remote Sens. Lett.* **2015**, *12*, 1735–1739. [[CrossRef](#)]
42. Shahzad, M.; Zhu, X. Robust Reconstruction of Building Facades for Large Areas Using Spaceborne TomoSAR Point Clouds. *IEEE Trans. Geosci. Remote Sens.* **2015**, *53*, 752–769. [[CrossRef](#)]
43. Schmitt, M.; Stilla, U. Compressive sensing-based layover separation in airborne single-pass multi-baseline InSAR data. *IEEE Geosci. Remote Sens. Lett.* **2013**, *10*, 313–317. [[CrossRef](#)]
44. Zhu, X.X.; Montazeri, S.; Gisinger, C.; Hanssen, R.F.; Bamler, R. Geodetic SAR Tomography. *IEEE Trans. Geosci. Remote Sens.* **2016**, *54*, 18–35. [[CrossRef](#)]
45. Ge, N.; Zhu, X. Bistatic-like Differential SAR Tomography—A Preliminary Framework for Tandem-L. *IEEE Trans. Geosci. Remote Sens.* **2018**. submitted.



© 2019 by the authors. Licensee MDPI, Basel, Switzerland. This article is an open access article distributed under the terms and conditions of the Creative Commons Attribution (CC BY) license (<http://creativecommons.org/licenses/by/4.0/>).